MHD and Thermal Simulations of a Radiation Cooled Self-field MPD Thruster

IEPC-2013-262

Presented at the 33rd International Electric Propulsion Conference,
The George Washington University • Washington, D.C. • USA
October 6 – 10, 2013

Akira Kawasaki[1]
Tokyo Institute of Technology, Yokohama, Kanagawa, 252-8502, Japan

Kenichi Kubota[2]
Japan Aerospace Exploration Agency, Chofu, Tokyo, 182-8522, Japan

Ikkoh Funaki[3]
Japan Aerospace Exploration Agency, Sagamihara, Kanagawa, 252-5210, Japan

and

Yoshihiro Okuno[4]
Tokyo institute of Technology, Yokohama, Kanagawa, 226-8502, Japan

Abstract: To develop a basic design guideline of a radiation cooled steady-state self-field magnetoplasmadynamic(MPD) thruster operated at several hundred kW electric power input with argon or hydrogen propellant, its configuration is preliminarily examined and its operation characteristics are simulated numerically. In particular, the influence of the cathode radius on the thrust performance and thruster temperature is investigated based on a combination of MHD simulation of plasma flow and thermal simulation of thruster components. It is revealed that the decrease in the cathode radius improves the thrust performance, but raises the electrode temperature locally at an anode exit edge and a cathode tip owing to the concentration of discharge current on them and insufficient heat removal. Thus, special attention should be paid to the temperature rise at the anode exit edge and the cathode tip in designing the thruster. Within a scope of this paper, a thrust of 16 N, a specific impulse of 4200 s, and a thrust efficiency of 41% are predicted to be achievable without electrode melting for the hydrogen propellant.

Nomenclature

B	=	magnetic flux density
$\boldsymbol{B}$	=	magnetic flux density vector
c_c	=	coefficient of wall heat flux on cathode
E	=	energy density
E_h	=	energy density of heavy particles
E_{rot}	=	energy density of molecular rotation
E_{tr}	=	energy density of molecular translation

[1] Graduate Student, Department of Energy Sciences, kawasaki.a.ac@m.titech.ac.jp
[2] Researcher, Institute of Aeronautical Technology, kkubota@chofu.jaxa.jp
[3] Associate Professor, Institute of Space and Astronautical Science, funaki@isas.jaxa.jp
[4] Professor, Department of Energy Sciences, yokuno@es.m.titech.ac.jp

E_{vib} = energy density of molecular vibration
e = elementary charge
F_{EM} = electromagnetic thrust
$\bar{I}$ = unit tensor
J_d = discharge current
$\boldsymbol{j}$ = current density vector
j_a = current density on anode
j_c = current density on cathode
k_B = Boltzmann constant
$\dot{m}$ = propellant mass flow rate
n = number density
n_e = electron number density
n_h = heavy particle number density
n_i = ion number density
n_s = number density of *s* species
p = (static) pressure
p_e = electron pressure
p_s = pressure of *s* species
Q = energy relaxation
Q^e_{diss} = energy loss of electron by dissociation
Q^e_{ion} = energy loss of electron by ionization
$Q_{e\text{-}vib}$ = energy relaxation from electron to molecule (vibration)
Q^h_{diss} = energy loss of heavy particles by dissociation
$Q_{tr\text{-}e}$ = energy relaxation from heavy particle (translation) to electron
$Q_{tr\text{-}vib}$ = energy relaxation from heavy particle (translation) to molecule (vibration)
q_a = heat flux on anode
q_c = heat flux on cathode
r = radius, radial coordinate
r_a = anode radius
r_c = cathode radius
S_{ion} = ion slip parameter
T = temperature
T_e = electron temperature
T_h = heavy particle temperature
T_{rot} = molecular rotational temperature
T_{tr} = heavy particle translational temperature
T_{vib} = molecular vibrational temperature
t = time
U = internal energy density
U_e = internal energy density of electron
$\boldsymbol{u}$ = velocity vector
V = voltage
$V_{a,conv}$ = equivalent voltage of convection in the vicinity of anode
$V_{a,sh}$ = sheath voltage of anode
$V_{c,sh}$ = sheath voltage of cathode
z = axial coordinate
α = electrode coefficient
β = (electron) Hall parameter
δE = energy relaxation from electron to heavy particle
ε = emissivity
θ_{vib} = characteristic vibrational temperature = 6320 K
λ = thermal conductivity
λ_h = thermal conductivity of heavy particles
λ_e = thermal conductivity of electron
λ_{rot} = thermal conductivity of molecular rotational energy
λ_{tr} = thermal conductivity of heavy particle translational energy

λ_{vib} = thermal conductivity of molecular vibrational energy
μ_0 = space permeability
ρ = density
ρ_s = density of *s* species
σ = electrical conductivity
$\bar{\tau}$ = viscous stress tensor
ϕ = work function
ϕ_a = work function of anode material

I. Introduction

NOWADAYS, activities in space are increasingly expanding toward deep space beyond earth orbits. Actually, a number of ambitious deep space missions are proposed and intensively investigated[1], e.g. explorations to the moon, asteroids, Mars and other celestial objects. Hereat, for those missions, the realization of a large electric propulsion system, which simultaneously improves the payload ratio and the mission time, is strongly demanded. Hence, it is an urgent task to develop such the large electric propulsion system which is available at a high input power exceeding several hundred kW and consequently exerts both high specific impulse and high thrust[2,3].

Magnetoplasmadynamic (MPD) thrusters are expected to be the most promising candidates of next generation's large electric propulsion systems. The MPD thruster can be operated solely without clustering even at the high input powers and is believed to diminish weight of the propulsion system. Although there are some categories among MPD thrusters, this paper particularly focuses on a steady-state self-field MPD thruster (hereafter, simply referred to as "MPD thruster") from the viewpoint of simplicity and performance potential.

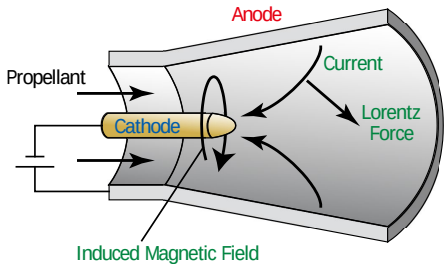

Figure 1. Operation concept of an MPD thruster.

Figure 1 shows the operation concept of the MPD thruster. To generate a thrust, the MPD thruster ionizes a propellant and accelerates it gas-dynamically and electromagnetically through a high-intensity arc discharge[4]. Thus, the thrust of the MPD thruster consists of two components: a gas-dynamic thrust attributed to Joule heating by the discharge current and an electromagnetic thrust attributed to the Lorentz force as the interaction between the discharge current and a magnetic field induced by the current. It is well known that the electromagnetic thrust is needed to be contributory enough for an efficient operation of the MPD thruster. Here, the theoretical value of the electromagnetic thrust is given by the Maecker formula[5]:

$$F_{EM} = \frac{\mu_0}{4\pi}\left(\ln\frac{r_a}{r_c} + \alpha\right)J_d^2 \tag{1}$$

Therefore anode-to-cathode radius ratio (hereafter, simply referred as "radius ratio") and discharge current are desired to be large enough. However, high-intensity discharge inevitably imposes a massive heat load onto the electrodes and extremely raises their temperature. If heat removal is incomplete, the electrodes will easily melt. Hence a careful thermal design, by which high performance is compatible with long-life operation, is indispensable for a practicable MPD thruster.

Until now, for relatively low-power classes of MPD thrusters, e.g. applied-field type or repetitive-pulse type, thruster design is established at a very high level. Actually, radiation cooled steady-state devices of applied-field MPD thruster[6-8] have been operated in laboratories and radiation cooled repetitive-pulse devices[9,10] have been demonstrated in space by the Institute of Space and Astronautical Science in Japan. However, as for a fully radiation cooled steady-state device of self-field MPD thruster which is operated at several hundred kW electric power input, its design is very challenging and has not been completely established although a partly radiation cooled steady-state device of self-field MPD thruster[11] is operated in a laboratory by the Institute of Space Systems (IRS) of University of Stuttgart.

In this paper, a basic design guideline of a practicable high-power MPD thruster operated at several hundred kW is developed. Firstly, for a radiation cooled steady-state devise of self-field MPD thruster using argon or hydrogen propellant, its configuration is preliminarily examined. Subsequently, for the obtained configuration, by varying a

cathode radius as a principal design parameter, its influence on thrust performance and electrode temperature is investigated based on a combination of MHD simulation of plasma flow and thermal simulation of thruster components. Additionally a design point where the thruster exerts a preferable performance without electrode melting is surveyed.

II. Configuration of Radiation Cooled Self-field MPD Thruster

A. Components and Heat Removal Paths

A configuration of a practicable high-power MPD thruster need to be examined preceding main subjects because there is no practicable device of such the thruster is obtained so far. For experiments in laboratories, MPD thrusters generally consist of an anode, a cathode, a cathode holder, and insulators and these components are arranged coaxially. The anode is commonly located surrounding the cathode owing to a difference in heat load amount between anode and cathode. The heat load amount is greater on the anode than on the cathode because electrons enter into the anode while the electrons are emitted from the cathode[12].

These heat loads should be removed in some way to avoid melting of the electrodes. For single-pulse quasi-steady-state operations in experiments, there is no need for special cooling system because inertial cooling is effective enough. On the other hand, for steady-state operations in experiments, water-cooling systems have been utilized[11], because it possess high heat removal capacity and can provide large safety margin to the overheat. The water-cooling system, however, is not adequate to actual space use, because, in space, the heat must be removed finally by the thermal radiation into deep space. Nevertheless, simple thermal radiation from the electrode surface (around 10^6 W/m^2 at most) is not always sufficient to prevent it from melting because the electrode of the high-power MPD thruster suffers from an extremely high heat flux exceeding 10^7 W/m^2 as will be shown later. Therefore, for a practical use of the thruster in space, an idea of heat removal from the electrodes by liquid metal heat pipes has been proposed[13], because they have high heat removal capability up to 10^7 W/m^2 [14]. In this paper, following the idea of utilization of heat pipes, an anode radiator, a cathode radiator and liquid metal heat pipes are added to the experimental device for a practical operation in space. Figure 2 shows a schematic view of a radiation cooled MPD thruster head. Here, the anode refers to the nozzle part and the anode radiator to disk-shaped part in this paper although the anode and the anode radiator are integrated.

In this configuration, heat flows within the thruster are to be as described below. As is shown in Fig. 2(b), the heat loaded on the anode inner surface is conducted within the anode toward its outer surface, then transferred to the anode radiator by anode heat pipes, and finally removed from the anode radiator. Similarly, as is also shown in Fig. 2(b), the heat loaded on the cathode is conducted within the cathode toward its root, then transferred to the distant cathode radiator by cathode heat pipes, and finally removed from the cathode radiator.

Heat regeneration to the propellants could not be effective in MPD thrusters because propellant flow rates are generally limited to small values for the sake of their efficient operations.

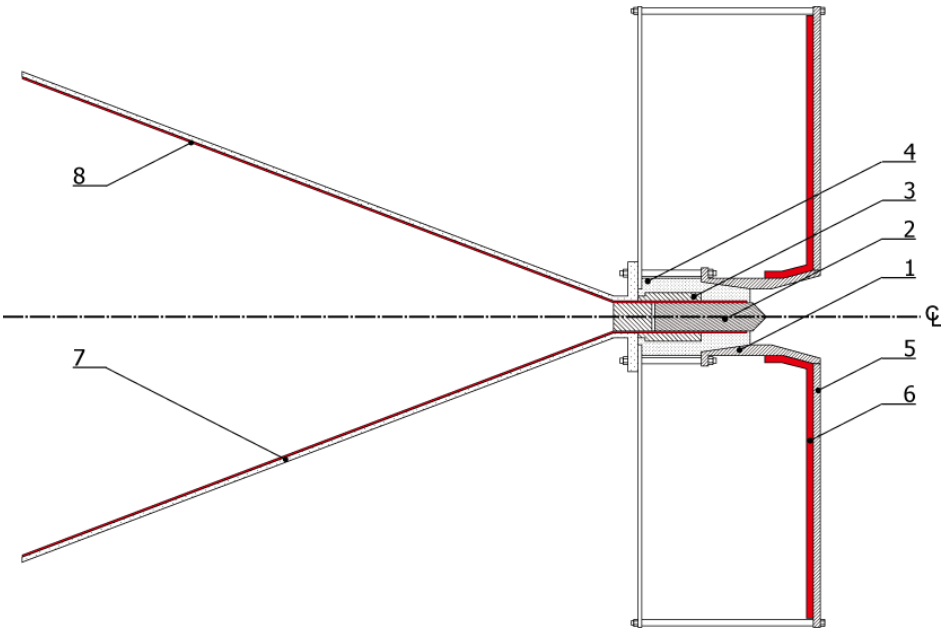

(a) Overall view

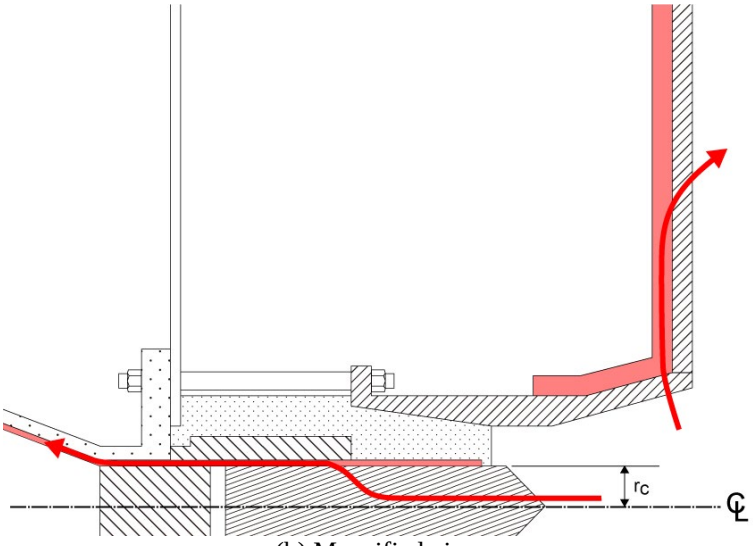

(b) Magnified view

Figure 2. Schematic of thruster head.
1 - Anode; 2 - Cathode; 3 - Cathode holder; 4 - Insulator;
5 - Anode radiator; 6 - Anode heat pipe; 7 - Cathode radiator; 8 - Cathode heat pipe.

B. Anode and Relating Parts

As for the anode, its operation temperature is desired to be as high as possible to reduce a required radiator area because higher anode temperature leads to higher radiator temperature and then higher radiation heat flux. Thus, as an anode material, tungsten is to be preferable from the viewpoint of available temperature range. According to the Maecker formula, larger anode inner radius, i.e. larger radius ratio, leads to higher performance, but too large anode inner radius could end up with unstable discharge owing to propellant rarefaction within the thruster, and consequently the deterioration of performance. Therefore, the anode inner radius is to be enlarged with keeping ionized propellant dens enough to provide a typical discharge current density (10^6 - 10^7 A/m^2). Anode wall is to be adequately thickened in order for the heat flux reaching the heat pipes not to concentrate locally, because heat flux

tends to be localized on the inner surface of the anode as is described below. The thick anode wall can avoid dryout of the heat pipes.

As for the anode heat pipe, its operation temperature is required to be as high as possible due to the same reason with anode. From the view point of high operation temperature and high heat removal capacity, lithium heat pipe is to be preferable. The anode heat pipes not only remove heat from the anode, but also can reduce thermal stress of the anode radiator owing to isothermalization of the anode radiator.

In the steady state, the heat load on the anode roughly equilibrates with the heat radiated from the anode radiator. The anode radiator radius is determined so as to keep the temperature of the heat pipe less than 2,000 K which is approximately the upper limit of operating temperature of the liquid-metal heat pipe[15].

C. Cathode and Relating Parts

As for the cathode, its operation temperature is also desired to be as high as possible from the view point of radiator temperature and thermionic electron emission. As a cathode material, thoriated tungsten has been usually utilized because it possesses both a high melting point and a low work function. From a viewpoint of overall heat transmission within the cathode toward the root, the cathode radius should be large adequately to avoid excessive heat flux, but from a viewpoint of thrust performance, it should be small to enhance magnetic thrust as can be seen from the Maecker formula. That is, there exists a design trade-off between the overall heat transmission capability and the thrust performance. Therefore, it is important to optimize the cathode radius.

The cathode also experiences high heat flux as with the anode. Thus, the utilization of heat pipes is also supposed for heat removal.

III. Numerical Model and Procedure

Steady-state operations of the MPD thruster are simulated with a combination of magnetohydrodynamic (MHD) and thermal simulation. Firstly the MHD analysis simulates the plasma flow, evaluates the thrust performance, and computes wall heat fluxes with considerations to electrode phenomena. Subsequently, the thermal analysis simulates temperature distribution of the thruster components suffering from the heat load computed by the MHD analysis.

D. MHD Fluid Phenomena of Plasma Flow

Steady-state plasma flows are simulated for argon or hydrogen propellant by an MHD flow solver which is being developed in authors' group[16]. In the simulation, MHD equations are solved with real gas effects: stoichiometric non-equilibrium, thermal non-equilibrium, the Hall effect, viscosity, thermal conduction, etc. The equations are discretized by the finite volume method. The convection terms and the diffusion terms are evaluated by the 2nd-order TVD Lax-Friedrichs scheme[17] or HLL scheme[18] and the 2nd-order central difference respectively. The steady-state solutions are obtained by the time marching with the explicit Euler method. Between simulation and experiment, fair agreement has been confirmed[19,20].

Argon Propellant

As for the argon propellant, neutral atoms and monovalent ions are considered as heavy particle species. A stoichiometric non-equilibrium is considered for ionizations. A thermal non-equilibrium is considered between heavy particle energy and electron energy (two temperature model). Basic equations are as follows: conservation equations of total mass

$$\frac{\partial \rho}{\partial t} + \nabla \cdot (\rho \boldsymbol{u}) = 0 \tag{2}$$

conservation equation of ion mass

$$\frac{\partial \rho_s}{\partial t} + \nabla \cdot (\rho_s \boldsymbol{u}) = \dot{\rho}_s \quad (s = \mathrm{Ar}^+) \tag{3}$$

conservation equation of momentum

$$\frac{\partial \rho \boldsymbol{u}}{\partial t} + \nabla \cdot (\rho \boldsymbol{u}\boldsymbol{u} + p\bar{\boldsymbol{I}}) = \nabla \cdot \bar{\tau} + \boldsymbol{j} \times \boldsymbol{B} \tag{4}$$

conservation equation of heavy particle total energy

$$\frac{\partial E_h}{\partial t} + \nabla \cdot \left[(E_h + p)\boldsymbol{u} \right] = p_e \nabla \cdot \boldsymbol{u} + \nabla \cdot (\bar{\boldsymbol{\tau}} \boldsymbol{u}) + \nabla \cdot (\lambda_h \nabla T_h) + \boldsymbol{u} \cdot (\boldsymbol{j} \times \boldsymbol{B}) + \delta E \tag{5}$$

conservation equation of electron internal energy

$$\frac{\partial U_e}{\partial t} + \nabla \cdot (U_e \boldsymbol{u}) = -p_e \nabla \cdot \boldsymbol{u} + \nabla \cdot \left(\lambda_e \nabla T_e + \frac{5}{2} \frac{k T_e}{e} \boldsymbol{j} \right) + \frac{\boldsymbol{j}^2}{\sigma} - \delta E - \dot{n}_i V_i \tag{6}$$

and induction equation

$$\frac{\partial \boldsymbol{B}}{\partial t} - \nabla \times (\boldsymbol{u} \times \boldsymbol{B}) = -\frac{1}{\mu_0 \sigma} \nabla \times \left[\nabla \times \boldsymbol{B} + \beta_e (\nabla \times \boldsymbol{B}) \times \frac{\boldsymbol{B}}{B} \right] \tag{7}$$

where, energy densities in the equations above are defined as follows

$$E_h = \frac{3}{2} n_h k_B T_h + \frac{1}{2} \rho \boldsymbol{u}^2 \tag{8}$$

$$U_e = \frac{3}{2} n_e k_B T_e \tag{9}$$

For the current density and the pressures, the following relations are assumed: Ampère's law

$$\boldsymbol{j} = \frac{1}{\mu_0} \nabla \times \boldsymbol{B} \tag{10}$$

and the equation of state of ideal gases

$$p = \sum_s p_s + p_e, \quad p_s = n_s k_B T_h, \quad p_e = n_e k_B T_e \quad \left(s = \mathrm{Ar}, \mathrm{Ar}^+ \right) \tag{11}$$

Hydrogen Propellant

As for the hydrogen propellant, molecules, neutral atoms, and monovalent ions are considered as heavy particle species. Stoichiometric non-equilibria are considered for dissociations and ionizations. Thermal non-equilibria are considered among heavy particle translational energy, molecular rotational energy, and electron energy (three temperature model). Additionally, ion slip is also considered. Basic equations are as follows: conservation equations of total mass

$$\frac{\partial \rho}{\partial t} + \nabla \cdot (\rho \boldsymbol{u}) = 0 \tag{12}$$

conservation equation of atom and ion mass

$$\frac{\partial \rho_s}{\partial t} + \nabla \cdot (\rho_s \boldsymbol{u}) = \dot{\rho}_s \quad \left(s = \mathrm{H}, \mathrm{H}^+ \right) \tag{13}$$

conservation equation of momentum

$$\frac{\partial \rho \boldsymbol{u}}{\partial t} + \nabla \cdot \left(\rho \boldsymbol{u}\boldsymbol{u} + p\bar{\boldsymbol{I}} \right) = \nabla \cdot \bar{\tau} + \boldsymbol{j} \times \boldsymbol{B} \tag{14}$$

conservation equation of heavy particle total energy

$$\begin{aligned} &\frac{\partial E_h}{\partial t} + \nabla \cdot \left[\left(E_h + p \right) \boldsymbol{u} \right] \\ &= p_e \nabla \cdot \boldsymbol{u} + \nabla \cdot \left(\bar{\tau} \boldsymbol{u} \right) + \nabla \cdot \left[\left(\lambda_{tr} + \lambda_{rot} \right) \nabla T_{tr} \right] + \nabla \cdot \left(\lambda_{vib} \nabla T_{vib} \right) + \boldsymbol{u} \cdot \left(\boldsymbol{j} \times \boldsymbol{B} \right) + S_{ion} \frac{\left(\boldsymbol{j} \times \boldsymbol{B} / B \right)^2}{\sigma} - Q_{tr-e} + Q_{e-vib} - Q_{diss}^h \end{aligned} \tag{15}$$

conservation equation of molecular vibrational energy

$$\frac{\partial E_{vib}}{\partial t} + \nabla \cdot \left(E_{vib} \boldsymbol{u} \right) = \nabla \cdot \left(\lambda_{vib} \nabla T_{vib} \right) + Q_{tr-vib} + Q_{e-vib} - Q_{diss}^h \tag{16}$$

conservation equation of electron internal energy

$$\frac{\partial U_e}{\partial t} + \nabla \cdot \left(U_e \boldsymbol{u} \right) = -p_e \nabla \cdot \boldsymbol{u} + \nabla \cdot \left(\lambda_e \nabla T_e \right) + \frac{\boldsymbol{j}^2}{\sigma} + Q_{tr-e} - Q_{e-vib} - Q_{diss}^e - Q_{ion}^e \tag{17}$$

and induction equation

$$\frac{\partial \boldsymbol{B}}{\partial t} - \nabla \times \left(\boldsymbol{u} \times \boldsymbol{B} \right) = -\frac{1}{\mu_0 \sigma} \nabla \times \left[\nabla \times \boldsymbol{B} + \beta_e \left(\nabla \times \boldsymbol{B} \right) \times \frac{\boldsymbol{B}}{B} + S_{ion} \left(\left(\nabla \times \boldsymbol{B} \right) \times \frac{\boldsymbol{B}}{B} \right) \times \frac{\boldsymbol{B}}{B} \right] \tag{18}$$

where, energy densities in the equations above are defined as follows

$$E_{tr} = \sum_{s=H_2, H, H^+} \frac{3}{2} n_s k_B T_{tr} \tag{19}$$

$$E_{rot} = n_{H_2} k_B T_{rot} = n_{H_2} k_B T_{tr} \tag{20}$$

$$E_{vib} = \frac{n_{H_2} k_B \theta_{vib}}{\exp\left(\theta_{vib} / T_{vib} \right) - 1} \tag{21}$$

$$E_h = E_{tr} + E_{rot} + E_{vib} + \frac{1}{2} \rho \boldsymbol{u}^2 \tag{22}$$

$$U_e = \frac{3}{2} n_e k_B T_e \tag{23}$$

For the current density and the pressure, the following relations are assumed: Ampère's law and the equation of state of ideal gases

$$p = \sum_s p_s + p_e, \;\; p_s = n_s k_B T_{tr}, \;\; p_e = n_e k_B T_e \;\; \left(s = \mathrm{H}_2, \mathrm{H}, \mathrm{H}^+ \right) \tag{24}$$

E. Electrode Phenomena

Phenomena in the vicinity of the electrodes, which are attributed to the existence of very thin electrode sheath, act important roles for the operation of the MPD thruster. Such electrode phenomena, however, are difficult to be

resolved directly by the MHD flow solver. Therefore, this paper takes into account the electrode phenomena such as sheath impedance and heat transfer through the sheath, by simplified models based on experimental suggestions.

The sheath impedances are considered by assuming constant sheath voltages based on past experimental measurements[21-23]. For the argon propellant, the sheath voltages are set to 0 V and 20 V at the anode and the cathode respectively. For the hydrogen propellant, the sheath voltages are set to 5 V and 40 V at the anode and the cathode respectively, where an electron sheath is assumed on the anode. For the performance evaluation, the sheath voltages are added to the discharge voltages obtained by the MHD simulation. The sheath voltages are also to affect the following models of wall heat flux on the electrodes.

Wall heat flux on the anode is evaluated by the equation below[24], considering heat transfer through the sheath.

$$q_a = \left(\frac{5}{2} \frac{kT_e}{e} + V_{a,sh} + \phi_a + V_{a,conv} \right) \cdot j_a \tag{25}$$

Where, the electron temperature is obtained by the MHD simulation. The work function is 4.5 V for tungsten. Influence of convection is assumed to be 2 V empirically. Similarly, wall heat flux on the cathode is evaluated by the equation below, based on an experiment[25] conducted by Hügel and Krülle.

$$q_c = c_c \cdot j_c \tag{26}$$

In the experiment, the coefficient of heat load decreased with the increase in the discharge current from 400 A to 1 kA. Hence, in this paper, the coefficient of heat load is set to the lower limit (1 W/A for the argon propellant and 0.7 W/A for the hydrogen propellant) because this study supposes discharge currents of well over 1 kA. This coefficient is thought to include the influence of the cathode sheath voltage and the convective heat transfer from the plasma implicitly.

F. Thermal Phenomena of Thruster Components

Steady-state temperatures of thruster components are simulated by the general-purpose finite element method solver MSC.Nastran[26]. In the simulation, the following conditions are assumed.

The dependencies of thermal properties such as thermal conductivity and emissivity on temperature[27] are considered. The heat fluxes computed by the MHD simulation of plasma flows are applied on the surfaces of the electrodes as heat load boundary conditions. Radiation boundary conditions are applied on the boundaries exposed to deep space (3 K), i.e. the inner surface of flared part of the anode, the outer surface of the anode, the surface of conical part of the cathode tip, the outer surface of the insulator and downstream surface of the anode radiator. In particular, on the downstream surface of the anode radiator, its emissivity is set to 0.6, under the assumption of a radiation-facilitating coat on the radiator's surface.

The anode heat pipes are treated as a highly conductive solid to simulate their operation. The effective thermal conductivity is set in a region corresponding to the heat pipes. Where, the value of thermal conductivity is calculated so that the following two thermal resistances become equal: a total thermal resistance of the actual heat pipe[28] (sum of heat resistances between outer wall and inner vapor at evaporation part and condensation part) and a thermal resistance of the imaginary solid. It has to be noted that the thermal conductivity used in this analysis is the azimuthally-averaged value, because, several heat pipes are to be radially arranged in an actual radiator. The operation of the cathode heat pipes is simulated by more simplified way. That is, temperature boundary condition is applied on the cathode root lateral surface.

G. Analysis Conditions and Thruster Dimensions

Analysis conditions are shown in Table 1. The discharge current and the propellant mass flow rate are determined so that the electromagnetic thrust is contributory enough.

Thruster dimensions are determined with consideration to the matters described in section II, as is shown in Table 2. The cathode radius is changed to survey parametrically its influence on thrust performance and electrode temperature, because the radius ratio is a principal design parameter as is seen from the Maecker formula.

Table 1. Analysis conditions.

Item	Condition	
Propellant	Ar	H_2
Discharge current J_d, kA	10	6
Propellant mass flow rate $\dot{m}$, g/s	1.8	0.4
MHD simulation		
Propellant temperature at thruster inlet, K	1000	600
Electrode model		
Anode sheath voltage $V_{a,sh}$, V	0	5
Cathode sheath voltage $V_{c,sh}$, V	20	40
Coefficient of cathode heat load c_c, W/A	1	0.7
Thermal analysis		
Anode wall heat flux	Eq. 25	
Cathode wall heat flux	Eq. 26	
Radiation from anode inner surf. (flared part) Radiation from anode outer surface	material- & temperature-dependent emissivity	
Radiation from cathode tip (conical part) Radiation from insulator outer surface		
Radiation from anode radiator (downstream)	$\varepsilon = 0.6$	
Cathode root temperature, K	300	
Anode HP effective thermal conductivity, W/m-K	28000	53000

Table 2. Thruster dimensions.

Item	Dimension	
Propellant	Ar	H_2
Anode inner radius at inlet r_a, mm	40	40
Anode inner radius at outlet, mm	59	64
Anode length, mm	100	120
- Cylindrical part, mm	30	30
- Flared part, mm	70	90
Cathode radius r_c, mm	12, 14, 16, 18, 20	8, 10, 12, 15, 20
Cathode length, mm	23	30
Cathode tip apex half-angle, deg	45	45
Anode radiator radius, mm	290	315

IV. Results and Discussion

H. Thrsut Performance and Plasma Flow

Figure 3 shows thrust and its breakdown as function of the cathode radius. As is shown in Fig. 3(a), the decrease in the cathode radius enhances mainly the electromagnetic thrust for the argon propellant. On the other hand, as is shown in Fig. 3(b), the decrease in the cathode radius enhances both the gas-dynamic thrust and the electromagnetic thrust for the hydrogen propellant.

The enhancements of the electromagnetic thrust are seen for both argon and hydrogen propellant. These are just the results as Maecker formula predicts. With the decrease in the cathode radius, magnetic flux density in the vicinity of the cathode is enhanced and resultantly blowing force (axial Lorentz force) is also enhanced. On the other hand, the enhancement of the gas-dynamic thrust is seen markedly for the hydrogen propellant. This is attributed to the enhancement of Joule heating. That is, the decrease in the cathode radius leads to the elongation of discharge current path and consequent increase in discharge voltage, because the electrode distance is increased and the Hall effect is enhanced (this will be described later). The reason why the enhancement of the gas-dynamic thrust is marked only for the hydrogen propellant, is that the attribution fractions of the gas-dynamic thrusts to the total thrusts are more significant for the cases of the hydrogen propellant because, for the hydrogen propellant, the discharge current is suppressed and the propellant is overfed to avoid unstable operation.

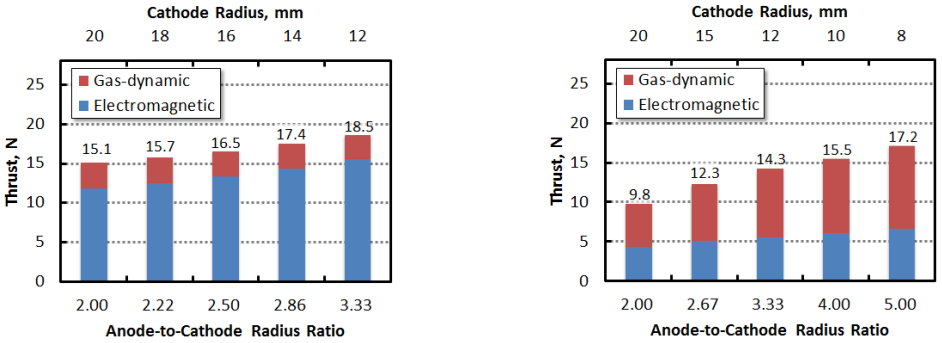

(a) Ar, J_d = 10 kA, $\dot{m}$ = 1.8 g/s (b) H_2, J_d = 6 kA, $\dot{m}$ = 0.4 g/s

Figure 3. Thrust and its breakdown as function of cathode radius[29,30].

Figure 4 shows specific impulse and thrust efficiency as function of cathode radius. The specific impulse and the thrust efficiency improve with the decrease in the cathode radius similarly to the thrust.

The improvements of the specific impulse are attributed to the enhancements of the thrust under the constant mass flow rates. As for the improvements of the thrust efficiency, it is because the enhancements of the thrust are more significant than the increases of input power. As for the difference between the argon and hydrogen propellant, this is attributed to their mass flow rate. For the hydrogen propellant, the mass flow rate to exert comparable thrusts with the argon propellant is small owing to the small atomic mass of hydrogen. Thus, in the case of the hydrogen propellant, the specific impulse is superior to the argon propellant and the thrust efficiency is also superior although the hydrogen propellant needs more input energy (as described later).

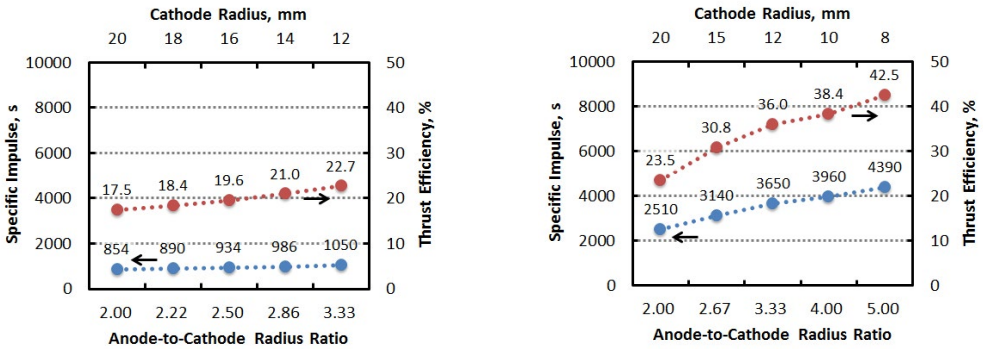

(a) Ar, J_d = 10 kA, $\dot{m}$ = 1.8 g/s (b) H_2, J_d = 6 kA, $\dot{m}$ = 0.4 g/s

Figure 4. Specific impulse and thrust efficiency as function of cathode radius[29,30].

Figure 5 shows the cathode radius dependency of Hall parameter and discharge current path. Qualitatively stated, Hall parameter and discharge current path behaves similarly for both argon and hydrogen propellant. In the case of thin cathode (small cathode radius), discharge current path is expanded downstream and elongated, compared to the case of thick cathode (large cathode radius). Discharge current path shifts toward the downstream region particularly on the anode and concentrate on the anode exit edge with the decrease in the cathode radius. As is also shown in Fig. 5, in the case of thin cathode, Hall parameter is greater than in the case of thick cathode.

Expanding of the discharge current path toward the downstream with the decrease in the cathode radius is attributed to the Hall effect. As is stated above, in the case of thin cathode (small cathode radius), Hall parameter is greater than in the case of thick cathode (large cathode radius). Thus, in the case of the thin cathode, the Hall effect affects and distorts current path more markedly. There are two reasons why Hall parameter rises in the case of thin cathode. One is that magnetic field is reinforced in the vicinity of the cathode (r ~ -12 to -20 mm and z ~ 0 to 30 mm for the argon or hydrogen propellant). The other is that density of heavy particles is lowered within the thruster. This lowering of density for the case of thin cathode is attributed to stronger acceleration of the propellant by the enhanced blowing force and pressure gradient, and stronger pinching of the propellant on the thruster axis by the enhanced pumping force (radial Lorentz force). In particular, for the case of the hydrogen propellant, influence of

the Hall effect is more marked because Hall parameter of the hydrogen propellant is greater than the argon propellant.

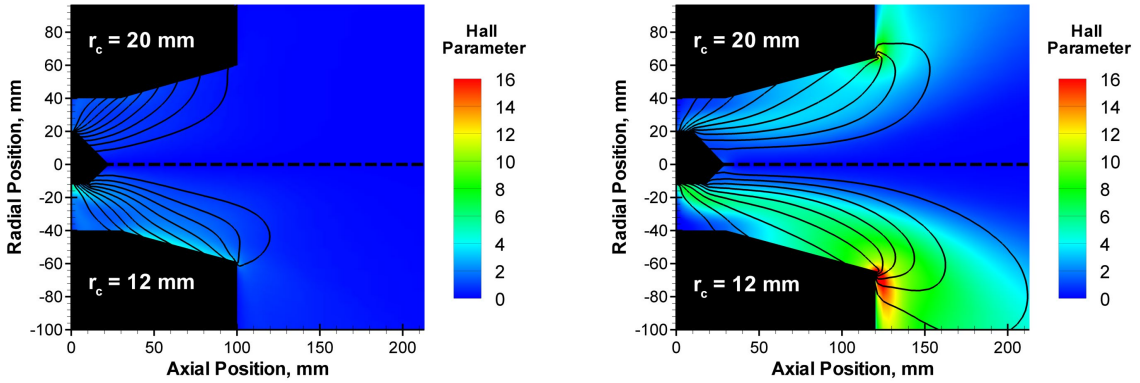

(a) Ar, J_d = 10 kA, $\dot{m}$ = 1.8 g/s (b) H_2, J_d = 6 kA, $\dot{m}$ = 0.4 g/s

Figure 5. Hall parameter and current path[29,30].

I. Heat Load on Electrodes

Figure 6 shows the cathode radius dependency of wall heat flux distribution on the anode. As for the anode, the wall heat flux concentrates on the exit edge (z ~ 100 mm for the argon propellant and z ~ 120 mm for the hydrogen propellant) and anode middle part (z ~ 10 to 30 mm) regardless of the cathode radius or propellant species. With the decrease in cathode radius, the wall heat flux decreases wholly except at the vicinity of the anode exit edge where wall heat flux rises markedly. This change in the wall heat flux distribution with the decrease in the cathode radius is attributed to the shift of the current path toward the downstream region.

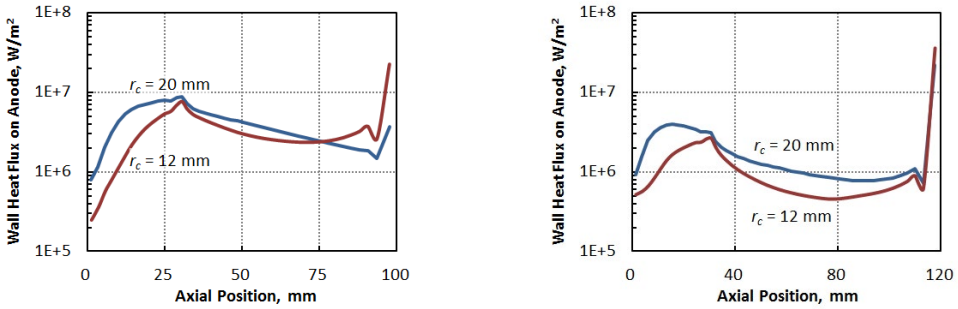

(a) Ar, J_d = 10 kA, $\dot{m}$ = 1.8 g/s (b) H_2, J_d = 6 kA, $\dot{m}$ = 0.4 g/s

Figure 6. Wall heat flux distribution on anode[29,30].

Figure 7 shows the cathode radius dependency of wall heat flux distribution on the cathode. As for the cathode, the wall heat flux increases at near-tip part with the decrease in the cathode radius. This change in the wall heat flux distribution with the decrease in the cathode radius is attributed to the decrease in the surface area of the cathode.

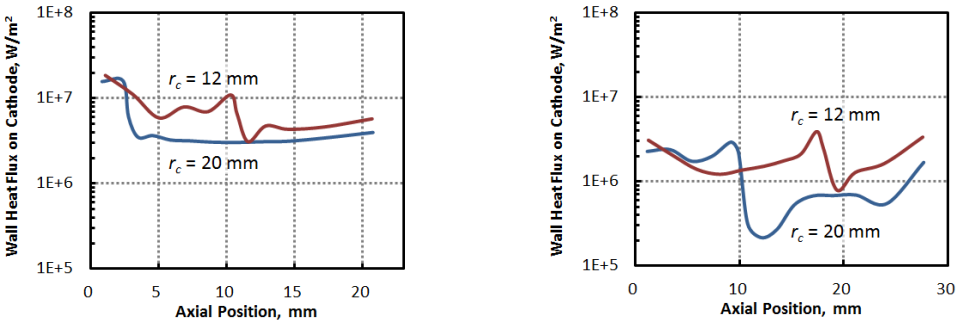

(a) Ar, J_d = 10 kA, $\dot{m}$ = 1.8 g/s (b) H_2, J_d = 6 kA, $\dot{m}$ = 0.4 g/s

Figure 7. Wall heat flux distribution on cathode[29,30].

Figure 8 shows the input power and the heat load on each electrode as function of the cathode radius. With the decrease in the cathode radius, the input power increases. For smaller cathode radius, the total heat load on the anode also increases slightly owing to the rise in electron temperature near the anode.

The increase in the input power with the decrease in the cathode radius is attributed to the rise in the discharge voltage owing to the expansion and the consequent elongation of the discharge current path. The slight increase in heat load on the anode with the decrease in the cathode radius is owing to the rise in electron temperature near the anode which results from stronger Joule heating associated with the expansion and the elongation of the discharge current path. The increase in input power is more marked for the hydrogen propellant because the expansion and elongation of the discharge current path is more marked for the hydrogen propellant.

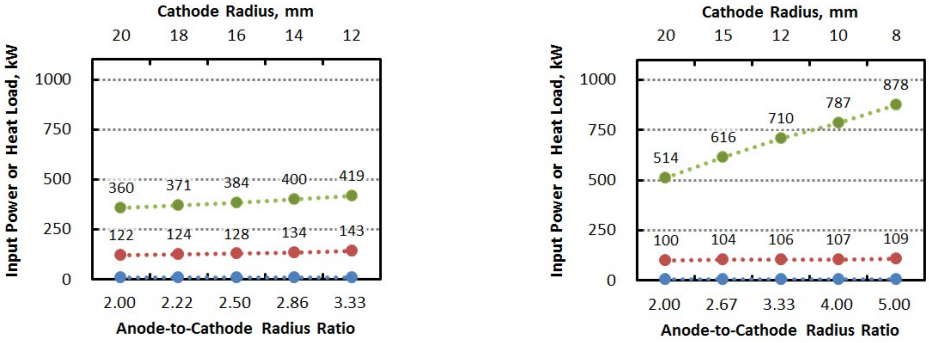

(a) Ar, J_d = 10 kA, $\dot{m}$ = 1.8 g/s (b) H_2, J_d = 6 kA, $\dot{m}$ = 0.4 g/s

Figure 8. Input power and heat load as function of cathode radius[29,30].

J. Electrode Temperature

Figure 9 shows a typical temperature distributions in the vicinity of the discharge chamber for the cathode radius of 12 mm. Notable temperature rises are seen commonly at the anode exit edges and the cathode tips regardless of the cathode radius.

Temperature rise at the anode exit edge is owing to the concentration of the wall heat flux (cf. Fig. 6). Temperature rise at the cathode tip can be explained by two reasons: one is that the heat flow is toward the root within the cathode because the heat is mainly removed from the root, and the other is that the cathode tip is tapered off for the sake of stable arc attachment. The temperature distribution of the thruster head indicates that temperatures at the anode exit edge and the cathode tip can be the limiting factors to determine thruster dimensions. That is, special attention should be paid to the temperatures of these regions to perform thermal design, and these temperatures must not exceed operating temperature limits of the materials.

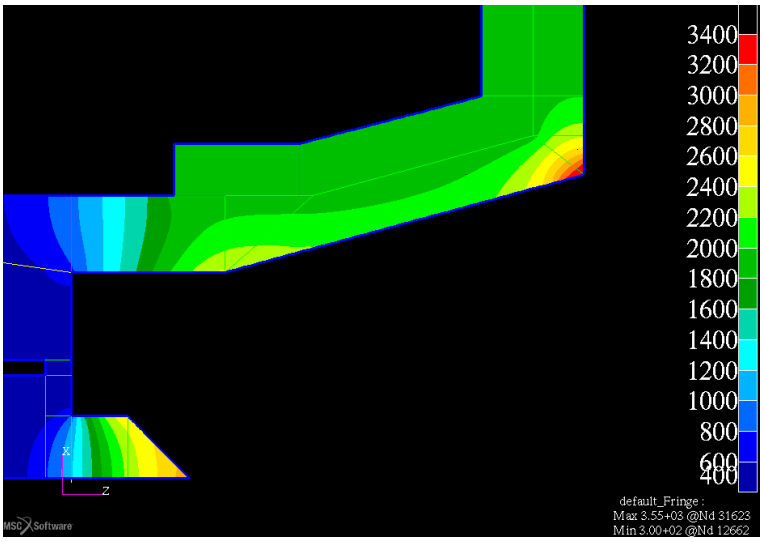

(a) Ar, J_d = 10 kA, $\dot{m}$ = 1.8 g/s, r_c = 12 mm

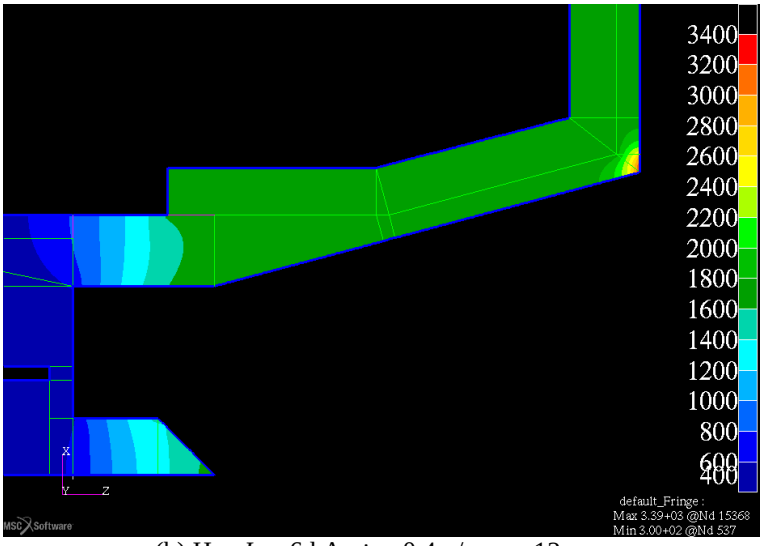

(b) H_2, J_d = 6 kA, $\dot{m}$ = 0.4 g/s, r_c = 12 mm

Figure 9. Typical temperature distribution in the vicinity of the discharge chamber.

Figure 10 shows electrode temperatures at the anode exit edge and the cathode tip as function of the cathode radius. With the decrease in the cathode radius, the temperature rises at the anode exit edge and the cathode tip becomes more marked.

The rise in the electrode temperatures at the anode exit edge and the cathode tip with the decrease in the cathode radius is the behavior which reflects the change in the heat flux distribution with the decrease in the cathode radius. The decrease in the cathode radius can incur thermally unfavorable situation although it leads to the improvement of thrust performance.

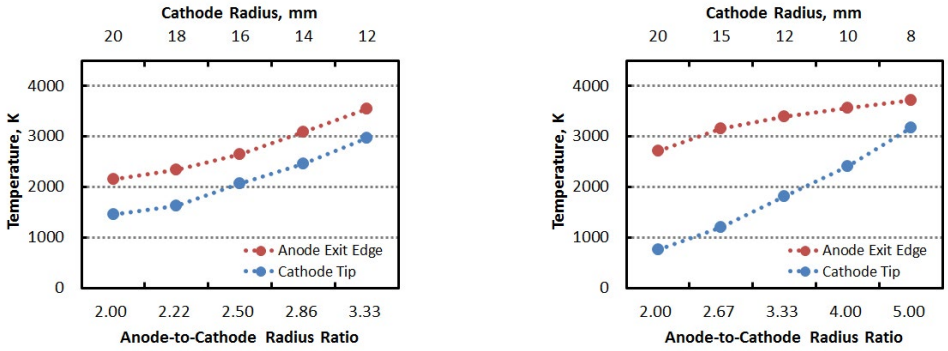

(a) Ar, J_d = 10 kA, $\dot{m}$ = 1.8 g/s (b) H_2, J_d = 6 kA, $\dot{m}$ = 0.4 g/s

Figure 10. Electrode temperatures as function of cathode radius[29,30].

For long life operation of the thruster, temperature of the anode (made of tungsten) should not exceed its melting point (~ 3670 K) and temperature of the cathode (made of thoriated tungsten) is recommended not to exceed 2800 K[24]. Under the assumptions and thermal constraints in this paper, the upper limits of estimated thrust performances are as follows. For the argon propellant, a thrust, a specific impulse and thrust efficiency are predicted to be 18 N, 1000 s, and 22% respectively with the cathode radius of 12.6 mm. For the hydrogen propellant, a thrust, a specific impulse and thrust efficiency are predicted to be 16 N, 4200 s and, 41% respectively with the cathode radius of 9.0 mm. Each value is estimated by the first-order interpolation among analysis cases. Also note that these performances are not necessarily to be the upper limits because there is still room for improvement with respect to other geometry parameters and operation conditions.

V. Conclusion

For a radiation cooled steady-state self-field MPD thruster using the argon or hydrogen propellant, thrust performance and electrode temperature have been investigated through performing sequential simulations of plasma flow and thruster temperature. As a result, the following conclusions have been drawn.

(1) A thruster without electrode melting can be realized by setting appropriate cathode radius and removing the heat from electrodes with the aid of liquid metal heat pipes.

(2) The temperature of the electrode rises particularly at the anode exit edge and the cathode tip owing to the concentration of discharge current and insufficient heat removal. Therefore the temperatures at these regions can be the limiting factors of thruster design.

(3) The decrease in the cathode radius improves thrust performance while it simultaneously furthers the temperature rising at the anode exit edge and cathode tip owing to more marked localization of heat flux. For the efficient and long-life operation of the MPD thruster, the cathode is to be designed with consideration of trade-off between the improvement of thrust performance and the localization of heat flux.

(4) Within the scope of this paper, the optimal cathode radii are 12.6 mm for the argon propellant and 9.0 mm for the hydrogen propellant. Then, thrust, specific impulse, and thrust efficiency are predicted to be 18 N, 1000 s, and 22% respectively for the argon propellant; 16 N, 4200 s, and 41% for the hydrogen propellant.

(5) The hydrogen propellant can be superior to the argon propellant with respect to thrust performance owing to its light mass. On the other hand, the hydrogen propellant can also incur more marked localization of heat flux on the anode exit edge than the argon propellant owing to intensive current concentration by the strong Hall effect.

As future works, the models of MHD fluid phenomena, electrode phenomena, and thermal phenomena have to be validated and refined through experiments, and those models have to be coupled and analyzed self-consistently to predict thrust performance and electrode temperature more precisely. Additionally, other geometry parameters, e.g. cathode length, anode inner diameter, anode length etc., and operation condition, e.g. discharge current, propellant flow rate, and cathode root temperature, should be optimized as an extension of this paper.

Acknowledgments

The authors appreciate fruitful discussion with Dr. Hiroki Sato.

References

[1]Bernhard Hufenbach, *et al*., "The Global Exploration Roadmap," *62nd International Astronautical Congress*, IAC-11.B3.1.8, Capetown, South Africa, 2013.

[2]Casaregola, C., Cesaretti, G., and Andrenucci, M., "HiPER: a Roadmap for Future Space Exploration with Innovative Electric Propulsion Technologies," *31st International Electric Propulsion Conference*, IEPC-2009-066, Ann Arbor, MI, 2009.

[3]Sankaran, K., Cassady, L., Kodys, A. D., and Choueiri, E. Y, "A Survey of Propulsion Options for Cargo and Piloted Missions to Mars," *Annuls New York Academy of Sciences*, Vol. 1017, No. 1, 2004, pp. 450-467.

[4]Jahn, R. G., *Physics of Electric Propulsion*, McGraw-Hill, New York, 1968.

[5]Maecker, H., "Plasmaströmungen in Lichtbögen Infolge eigen- magnetischer Kompression," *Z. Physik* (in German), Vol. 141, No. 1-2, 1955, pp. 198-216.

[6]Seikel, G. R., York, T. M., and Condit, W. C., "Roles for Magnetic Thrusters in Orbit-Rising Missions," SciTec, SciTec-Report. 8203, 1982.

[7]Krülle, G., "Continuous MPDA Development Status," *3rd European Electric Propulsion Conference*, Cologne, Germany, 1974.

[8]Tikhonov, V., Semenikhin, S., Brophy, J. R., and Polk, J. E., "The Experimental Performances of the 100kW Li MPD Thruster within an External Magnetic Field," *24th International Electric Propulsion Conference*, IEPC-95-105, Moscow, Russia, 1995.

[9]Kuriki, K., Kawashima, N., Sasaki, S., Yanagisawa, M., and Obayashi, T., "Space Experiment with Particle Accelerators (SEPAC) performed in Spacelab First," *18th International Electric Propulsion Conference*, AIAA Paper 85-1996, Alexandria, VA, 1985.

[10]Toki, K., Y. Shimuzu, and K. Kuriki. "Electric propulsion experiment (EPEX) of a repetitively pulsed MPD thruster system onboard space flyer unit (SFU)," *25th International Electric Propulsion Conference*, IEPC-97-120, Cleveland, OH, 1997.

[11]Herdrich, G., et. al., "Overview on Electric Propulsion Development at IRS," *32nd International Electric Propulsion Conference*, IEPC 2011-134, Wiesbarden, Germany, 2011.

[12]Shin, K. T. and Pfender, E., "Electrode Energy Transfer Mechanisms in a MPD Arc," *AIAA Journal*, Vol. 8, No. 2, 1970, pp. 211-215.

[13]Sercel, J. C., and Krauthamer, S., "Multimegawatt Nuclear Electric Propulsion - First Order System Design and Performance Evaluation," *AIAA Space Systems Technology Conference*, AIAA Paper 86-1202, San Diego, CA, 1986.

[14]Rosenfeld, J. H. and North, M. T., "Porous Media Heat Exchangers for Cooling of High-Power Optical Components," *Optical Engineering*, Vol. 34, No. 2, 1995, pp. 335-341.

[15]Ernst, D. M. and Eastman, G. Y., "High Temperature Heat Pipe Technology at Thermacore - An Overview," *AIAA 20th Thermophysics Conference*, AIAA Paper 85-0981, Williamsburg, VA, 1985.

[16]Kubota, K., Sato, H., Funaki, I. and Okuno, Y., "Magnetohydrodynamic simulation of MPD thruster," *Journal of the Japan Society for Aeronautical and Space Sciences* (in Japanese), Vol. 59, 2011, pp. 396-401.

[17]Tóth, G., and Odstčril, D. "Comparison of Some Flux Corrected Transport and Total Variation Diminishing Numerical Schemes for Hydrodynamic and Magnetohydrodynamic Problems," *Journal of Computational Physics*, Vol. 128, No. 1, 1996, pp. 82-100.

[18]Harten, A., Lax, P. D., and van Leer, B., "On Upstream Differencing and Godunov-type Schemes for Hyperbolic Conservation Laws," *SIAM Review*, Vol. 25, No. 1, 1983, pp. 35-61.

[19]Kubota, K., Funaki, I., and Okuno, Y. "Comparison of Simulated Plasma Flow Field in a Two-Dimensional Magnetoplasmadynamic Thrsuter With Experimental Data," *IEEE Transactions on Plasma Science*, Vol. 37, No. 12, 2009, pp. 2390-2398.

[20]Sato, H., Kubota, K. and Funaki, I., "Numerical Simulation of Hydrogen Plasma Flow within a Two-Dimensional Magnetoplasmadynamic Thruster using Self-field," *53rd Conference on Aerospace Propulsion and Power* (in Japan), JSASS-2013-0028 (in Japanese), Kurashiki, Okayama, 2013.

[21]Auweter-Kurtz, M., Habiger, H., Kurtz, H., Schrade, H., and Sleziona, C. "High Power Steady State MPD Thrusters," Institut für Raumfahrtsysteme, Universität Stuttgart, IRS-90-P4, Final Report, Grant US AFOSR-88-0325, Mar.1990.

[22]Nakata, D., Toki, K., Funaki, I., Shimizu, Y., Kuninaka, H. and Arakawa, Y., "Experimental Measurement of Total Sheath Fall Voltage in an MPD Thruster," *44th Joint Propulsion Conference & Exhibit*, AIAA Paper 2008-4635, Hartford, CT, 2008.

[23]Kuriki K., Onishi, M., and Morimoto, S., "Thrust Measurement of KIII MPD Arcjet," *AIAA Journal*, Vol. 20, No. 10, 1982, pp. 1414-1419.

[24]Bruno, C., *Nuclear Space Power and Propulsion Systems*, AIAA Inc., Reston, VA, 2008.

[25]H ügel, H., and Krülle, G., "Phänomenologie und Energiebilanz von Lichtbogenkathoden bei niedrigen Drucken und Hohen Stromstärken," *Beiträge aus der Plasmaphysik* (in German), Vol. 9, No. 2, 1969, pp. 87-116.

[26]MSC Nastran, Ver. 2012, MSC Software, Santa Ana, CA, 2012.

[27]Touloukian, Y. S., *Thermophysical Properties of High Temperature Solid Materials*, Macmillan, New York, 1967.

[28]Reay, D. A., and Kew, P. A., *Heat Pipes*, Butterworth-Heinemann, Oxford, 2006.

[29]Kawasaki, A, Kubota, K., Funaki, I. and Okuno, Y., "Thermal Design of a Self-field Argon MPD Thruster by Numerical Calculation," *Transactions of the Japan Society for Aeronautical and Space Sciences* (in Japanese) (to be published).

[30]Kawasaki, A., Kubota, K., Funaki, I. and Okuno, Y., "MHD Simulation and Thermal Design of an MPD Thruster," *29th International Symposium on Space Technology and Science*, 2013-s-101-b**,** Nagoya, Japan, 2013.